

Self-Limiting Temperature Window for Thermal Atomic Layer Etching of HfO_2 and ZrO_2 Based on the Atomic-Scale Mechanism

Rita Mullins^{II}, Suresh Kondati Natarajan,^{II} Simon D. Elliott, and Michael Nolan*



Cite This: *Chem. Mater.* 2020, 32, 3414–3426



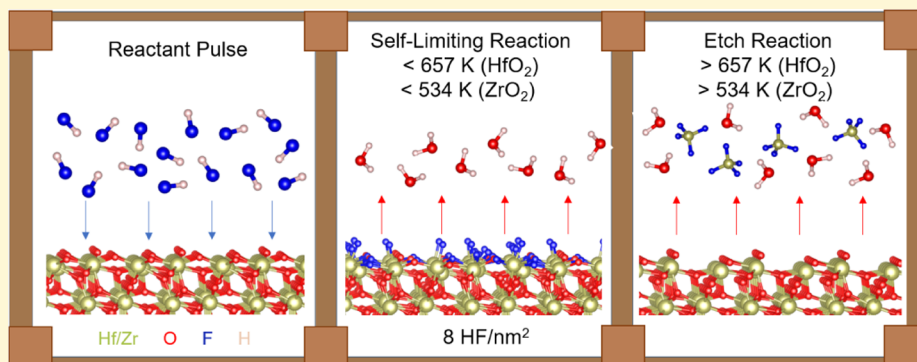
Read Online

ACCESS |

Metrics & More

Article Recommendations

Supporting Information



ABSTRACT: HfO_2 and ZrO_2 are two high- k materials that are important in the downscaling of semiconductor devices. Atomic-level control of material processing is required for the fabrication of thin films of these materials at nanoscale device sizes. Thermal atomic layer etching (ALE) of metal oxides, in which up to one monolayer of the material can be removed, can be achieved by sequential self-limiting (SL) fluorination and ligand-exchange reactions at elevated temperatures. However, to date, a detailed atomistic understanding of the mechanism of thermal ALE of these technologically important oxides is lacking. In this paper, we investigate the hydrogen fluoride (HF) pulse in the first step in the thermal ALE process of HfO_2 and ZrO_2 using first-principles simulations. We introduce Natarajan–Elliott analysis, a thermodynamic methodology, to compare reaction models representing the self-limiting (SL) and continuous spontaneous etching (SE) processes taking place during an ALE pulse. Applying this method to the first HF pulse on HfO_2 and ZrO_2 , we found that thermodynamic barriers impeding continuous etching are present at ALE-relevant temperatures. We performed explicit HF adsorption calculations on the oxide surfaces to understand the mechanistic details of the HF pulse. A HF molecule adsorbs dissociatively on both oxides by forming metal–F and O–H bonds. HF coverages ranging from 1.0 ± 0.3 to $17.0 \pm 0.3 \text{ HF/nm}^2$ are investigated, and a mixture of molecularly and dissociatively adsorbed HF molecules is present at higher coverages. Theoretical etch rates of $-0.61 \pm 0.02 \text{ \AA/cycle}$ for HfO_2 and $-0.57 \pm 0.02 \text{ \AA/cycle}$ for ZrO_2 were calculated using maximum coverages of 7.0 ± 0.3 and $6.5 \pm 0.3 \text{ M–F bonds/nm}^2$, respectively ($\text{M} = \text{Hf}, \text{Zr}$).

INTRODUCTION

The scaling of semiconductor devices means that features are required at the nanometer scale. As a result of the shrinking of device feature sizes, SiO_2 gate dielectrics would be so thin that electron tunneling through the dielectric layer, which leads to high leakage currents,¹ is impossible to avoid. Materials with high dielectric constant, k , allow a high drive current to be maintained, while minimized leakage current and a low equivalent oxide thickness can be achieved.¹ HfO_2 and ZrO_2 are high- k dielectric materials with dielectric constants of 22–23,^{1,2} which are used in semiconductor devices. HfO_2 and ZrO_2 are also thermodynamically stable when interfaced with silicon in semiconductor applications.³ However, conformal nanometer-scale feature sizes in high-aspect-ratio structures are difficult to achieve with traditional wet and dry chemical etching methods, which do not permit the level of control required. Recently, atomic layer etching (ALE) has gained

significant interest for the controlled etching of thin films, in particular, for nanoelectronic devices. ALE shares many features with atomic layer deposition (ALD) and can be considered as the reverse of ALD. ALE permits the removal of thin films with atomic-scale precision using sequential and self-limiting (SL) surface reactions,^{4–9} similar to ALD.

Traditional ALE processes are anisotropic as they use directional high-energy ion bombardment to remove the modified surface layer.⁶ Thermal ALE relies on temperature

Received: December 5, 2019

Revised: April 1, 2020

Published: April 2, 2020



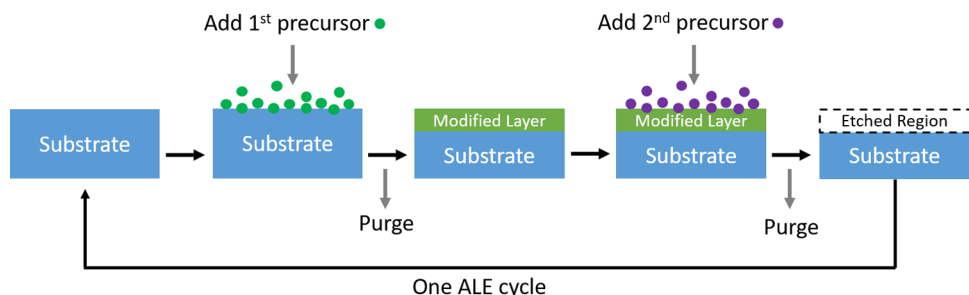


Figure 1. Schematic model of the thermal ALE process.

and thermochemically favorable reactions to remove surface species.¹⁰ While there have been many examples of thermal ALE of a range of materials, including HfO_2 ,^{4,9,11,124,9,11,12 ZrO_2 ,¹³ SiO_2 ,¹³ Al_2O_3 ,^{12,14–18} AlN ,¹⁹ AlF_3 ,²⁰ TiO_2 ,²¹ TiN ,^{22,23} W ,^{24,25} WO_3 ,²⁵ ZnO ,²⁶ and GaN ,²⁷ and for other ALE techniques including Ar neutral beam ZrO_2 ,²⁸ plasma ALE SiO_2 ,^{29,30} ZnO ,³¹ GaN ,^{32,33} and ALE of Si_3N_4 ,³⁴ using infrared annealing, the details of the mechanism of the ALE process still require significant work to understand.}

The first step in ALE is the formation of a reactive but nonvolatile layer on the initial film, which is followed by a material removal step to take off only the modified layer as indicated schematically in Figure 1. The key aspect of the ALE process is the self-limiting modification of the pristine film with the first precursor to produce a thin nonvolatile surface layer. The purpose of this modification step is to form a reactive, but nonvolatile, layer that can be easily removed in the subsequent ligand-exchange step.^{6,35} To date, reactions during thermal ALE are based on gas-phase fluorination that converts the metal-containing film into a layer of the corresponding nonvolatile metal fluoride.^{4,7,11} For metal oxides, thermal ALE processes generally use HF for the fluorination step.²² HF is a useful nucleophilic fluorination reactant in which the fluoride anion serves as the active reaction species.³⁶ This modification step in thermal ALE is the focus of this paper.

The other half of the thermal ALE cycle consists of a ligand exchange between a metal precursor and the newly formed fluoride layer at elevated temperatures,^{4,7,11} for which examples include $\text{Sn}(\text{acac})_2$,⁴ $\text{Al}(\text{CH}_3)_3$,^{4,37} $\text{Al}(\text{CH}_3)_2\text{Cl}$,⁴ SiCl_4 ,⁴ TiCl_4 ,¹¹ BCl_3 ,²¹ and WF_6 .²⁴ This second reaction produces stable etch products, which are now volatile³⁶ and can be easily removed, leaving behind a film from which one layer or a fraction of a layer has been removed as shown schematically in Figure 1. Repeating this cycle results in controlled removal of layers from the original film. Other applications of thermal ALE include surface cleaning for the removal of metal impurities in semiconductor fabrication, conformal etching in high-aspect-ratio structures, and smoothing of surfaces to obtain flat and damage-free layers, which are also important in the semiconductor industry.^{7,38} Therefore, thermal ALE is a strong candidate as a processing technology in current and future semiconductor device fabrication.³⁷

Given that it is difficult to investigate the ALE reactions directly using experimental techniques, first-principles-based atomic-level simulations using density functional theory (DFT) can give deep insights into the precursor chemistry and the reactions that drive the etch of metal oxides. In this paper, the hydrogen fluoride (HF) pulse in the first step in thermal ALE of HfO_2 and ZrO_2 using DFT calculations will be examined. HF molecules adsorb at the surfaces of metal oxides

by forming metal–F bonds, and there can also be hydrogen bonds between HF molecules. In addition, adsorbed HF may remain intact or dissociate. In the latter case, Hf–F/Zr–F and O–H are formed on HfO_2 and ZrO_2 , similar to that in recent work on Al_2O_3 etch modeling.³⁹ The amount etched (etch rate) is determined by how much of the oxide surface is fluorinated and how much of the metal fluoride can be removed in the ligand exchange for one ALE cycle.⁴

In addition to investigating HF adsorption, we introduce Natarajan–Elliott analysis (N–E analysis, in short) to predict the conditions at which a self-limiting (SL) or continuous spontaneous etch (SE) reaction becomes thermodynamically favorable, subject to kinetic barriers. This information is useful for directing experimental studies of thermal ALE. Self-limiting reactions are a necessary part of thermal ALE and allow the degree of etching to be well controlled and defined. We find that SL reactions are more favorable than the competing SE reactions for the HF pulse on HfO_2 and ZrO_2 at 0 K. The temperatures above which spontaneous etching is favored are 657 and 534 K for HfO_2 and ZrO_2 , respectively, at typical thermal ALE reactant pressures. Introducing one HF molecule to the bare surfaces of HfO_2 and ZrO_2 results in dissociative adsorption irrespective of the binding site. We determine the maximum coverage of metal–F bonds on the surface and use this coverage to calculate a theoretical etch rate. We also determine the maximum etch rate computed from the lattice constants of HfO_2 and ZrO_2 for one monolayer (ML) removal of Hf/Zr. We compare this maximum etch rate to experimental etch rates to calculate the number of Hf/Zr removed per surface area. We study the spontaneous formation of water that resulted from some of our relaxed geometries. This combined thermodynamic and mechanistic investigation using the first-principles simulation allows us to understand and design novel ALE processes for other technologically relevant materials. We first present a thermodynamic analysis that shows that the fluorinated surface is preferred over the oxygen fluoride and then present a detailed analysis of the adsorption coverage of HF molecules at HfO_2 and ZrO_2 , which allows us to also predict etch rates and number of metal atoms removed in a cycle.

■ COMPUTATIONAL METHODS

All reported surface slab calculations in this paper are performed using spin-polarized density functional theory as implemented in the VASP⁴⁰ 5.4 package. The calculations are based on the generalized gradient approximation (GGA) using the Perdew–Burke–Ernzerhof (PBE) exchange–correlation (XC) functional.⁴¹ The self-consistent energy for the electronic minimization is converged within 1×10^{-4} eV, and the forces for ionic relaxation are converged within -2×10^{-2} eV/Å. The default smearing method of Methfessel–Paxton first order is used with 0.1 eV broadening for electronic relaxation. The core

electrons are described by projector-augmented wave (PAW) potentials,⁴² and the valence electrons (Hf: 6s² 5d², Zr: 5s² 4d², O: 2s² 2p⁴, F: 2s² 2p⁵, and H: 1s¹) are treated using plane-wave basis sets with a kinetic energy cutoff of 400 eV. For configurations 2HF B for HfO₂ and ZrO₂, we include the tag IVDW = 20 for the Tkatchenko–Scheffler scheme in our INCAR. We found that their adsorption energies were increased only by \approx 0.05 eV by including this dispersion method and therefore we do not include it in the below analysis.

Relating SL and SE Processes: N–E Analysis. The relationship between SE and SL processes of a substrate exposed to a single gaseous reactant is described schematically in Figure 2. In an SL

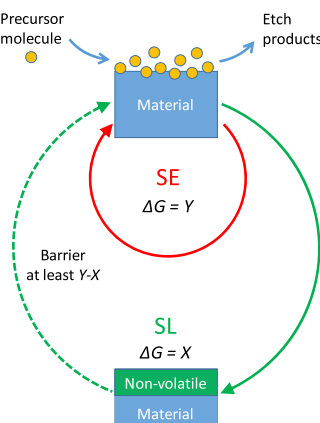
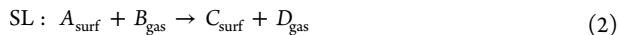


Figure 2. Schematic representation of the relationship between continuous spontaneous etch (SE, red) and self-limiting (SL, green) processes. ΔG represents the reaction free energy.

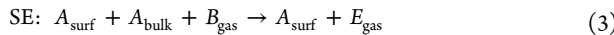
reaction, represented by the solid green arrow in Figure 2, the reactant molecules passivate the material surface and form a nonvolatile layer that resists further reaction. Such a reaction is referred to as a “surf \rightarrow surf” reaction



with the reaction free energy defined as $\Delta G = X$. Here, the starting surface A is necessarily different from the final surface C. It is possible that byproducts are released into the gas phase during this reaction



Conversely, in a SE reaction (represented by the solid red arrow in Figure 2), the reactant molecules etch away units of bulk material continuously by forming stable and volatile etch byproducts. This continues until the supply of the reactant gas molecules is stopped or the substrate material is exhausted (e.g., an etch stop is reached). Such a reaction is referred to as a “bulk \rightarrow gas” reaction



with the reaction free energy $\Delta G = Y$. Clearly, Y is independent of A_{surf} .

The reaction free energy ΔG at temperature T is computed as

$$\Delta G = \Delta H - T\Delta S + RT \ln(Q) \quad (5)$$

$$\Delta H = \Delta E + \Delta ZPE + \Delta W(T) \quad (6)$$

$$\Delta E = \sum_p \mu E_p - \sum_r \mu E_r \quad (7)$$

$$Q = \prod p_{\text{products}}^\mu / \prod p_{\text{reactants}}^\mu \quad (8)$$

In eq 5, ΔH and ΔS represent the changes in reaction enthalpy and reaction entropy, respectively. Since the partial pressures of the reactants and products are variable in the reaction chamber, the $RT \ln(Q)$ term is included. ΔH in eq 6 includes three contributions, namely, electronic reaction energy ΔE , zero-point energy change ΔZPE , and a temperature-dependent enthalpic contribution $\Delta W(T)$. While the reaction energy (ΔE) in eq 7 includes only the bonding information at temperature $T = 0$ K, the reaction free energy (ΔG) provides finite temperature and pressure behavior of a particular reaction. In eq 7, μ refers to the stoichiometric coefficient of the corresponding species and indices r and p indicate reactant and product species, respectively. The reaction quotient Q includes partial pressures of the gas-phase reactant and product molecules only. If the reactant and product pressures are the same, then $\ln Q$ becomes 0. A negative ΔS increases the free energy and tends to make the reaction more endergonic. Via the translational entropy, the value of ΔS is strongly dependent on the difference in molecularity between the products and the reactants. For example, if the number of gaseous molecules in the products is considerably smaller than in the reactants, then the ΔS value is likely to be negative and to result in an increase in the reaction free energy. In this work, we also evaluate the contribution from changes in surface entropy.

A negative value of ΔG means that the corresponding reaction is exergonic (favorable); otherwise, it is endergonic (unfavorable). The ΔG values are based on the SE and SL reactions as thermochemically isolated processes. However, we find it useful to consider also the overall energetics of the reaction pathway that theoretically links SL to SE (the green dotted line in Figure 2). It may be possible to form SE reaction products from the SL reaction products by overcoming one or several energetic barriers. While it is possible to compute kinetic barriers at the first-principles level, we omit this in favor of developing a computational approach that allows rapid screening. Balancing the energies in Figure 2 shows that these unknown barriers must be of magnitude at least $Y - X$ (free energy difference of SL and SE

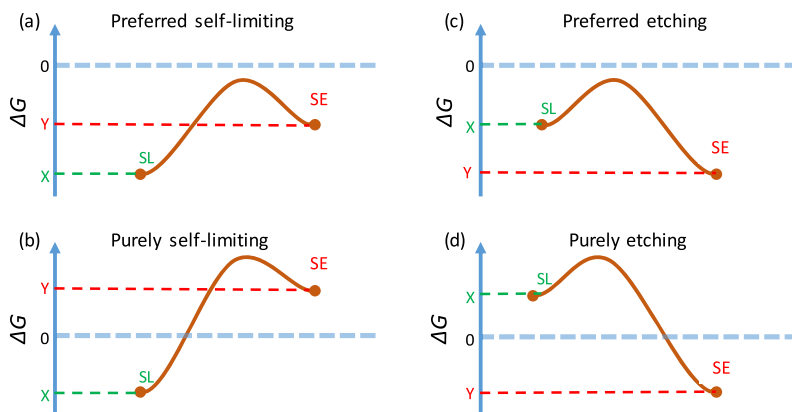


Figure 3. Schematic energy profiles representing (a) preferred self-limiting, (b) purely self-limiting, (c) preferred etching, and (d) purely etching.

Table 1. Reaction Energies ΔE at 0 K and Reaction Free Energies ΔG at 500 K of the Model SE and SL Reactions Representing the HF Pulse on HfO_2 and ZrO_2 ^a

		reactions	ΔE (eV/M)	ΔG (eV/M)
HfO_2				
SE1		$1\text{HfO}_{2(\text{b})} + 4\text{HF}_{(\text{g})} \rightarrow 1\text{Hff}_{4(\text{g})} + 2\text{H}_2\text{O}_{(\text{g})}$	-0.91	-0.65
SL1		$1\text{HfO}_{2(\text{surf})} + 4\text{HF}_{(\text{g})} \rightarrow 1\text{Hff}_{4(\text{surf})} + 2\text{H}_2\text{O}_{(\text{g})}$	-3.27 (2.36)	-1.20 (0.55)
SE2		$1\text{HfO}_{2(\text{b})} + 2\text{HF}_{(\text{g})} \rightarrow 1\text{HfOF}_{2(\text{g})} + 1\text{H}_2\text{O}_{(\text{g})}$	3.87	3.10
SL2		$1\text{HfO}_{2(\text{surf})} + 2\text{HF}_{(\text{g})} \rightarrow 1\text{HfOF}_{2(\text{surf})} + 1\text{H}_2\text{O}_{(\text{g})}$	-1.64 (5.51)	-0.60 (3.70)
ZrO_2				
SE1		$1\text{ZrO}_{2(\text{b})} + 4\text{HF}_{(\text{g})} \rightarrow 1\text{Zrf}_{4(\text{g})} + 2\text{H}_2\text{O}_{(\text{g})}$	-1.14	-0.89
SL1		$1\text{ZrO}_{2(\text{surf})} + 4\text{HF}_{(\text{g})} \rightarrow 1\text{Zrf}_{4(\text{surf})} + 2\text{H}_2\text{O}_{(\text{g})}$	-3.04 (1.90)	-1.00 (0.11)
SE2		$1\text{ZrO}_{2(\text{b})} + 2\text{HF}_{(\text{g})} \rightarrow 1\text{ZrOF}_{2(\text{g})} + 1\text{H}_2\text{O}_{(\text{g})}$	2.96	2.19
SL2		$1\text{ZrO}_{2(\text{surf})} + 2\text{HF}_{(\text{g})} \rightarrow 1\text{ZrOF}_{2(\text{surf})} + 1\text{H}_2\text{O}_{(\text{g})}$	-1.52 (4.48)	-0.50 (2.69)

^aThe value within parenthesis corresponds to the minimum barrier between the respective SE and SL reactions. The product state of SL1 and SL2 reactions is the 8O/16F surface of MO_2 ($\text{M} = \text{Hf/Zr}$) as described in the previous section, and the reaction energy is listed per the modified M atom.

reactions) in energy units. This term $Y - X$ will be referred to as the “minimum barrier” in this paper.

Based on the values of X and Y , we can distinguish the four possible scenarios for the precursor pulse shown in Figure 3. Each profile in Figure 3 depicts a set of SL and SE reaction free energies separated by unknown energetic barriers, which in reality may consist of many barriers in the configurational space of the system. Computing all of the reaction pathways and barriers separating the SL and SE product states would be computationally demanding. The aim of this methodology is to form useful conclusions without computing these pathways, thus accelerating process design. The minimum possible barrier to drive the etch reaction from the SL to SE product state is $Y - X$ in energy units as mentioned earlier. In the energy profiles, the SL reaction appears on the left-hand side of the horizontal axis since the precursor molecules must first react with the surface before accessing the bulk. To cause etching from there onward, the precursor molecules may have to lift the surface atoms out of their lattice positions or diffuse into the subsurface region and finally form volatile products. Therefore, the SE reaction is shown to the right of the SL reaction in these energy profiles.

Depending on whether the SL reaction or the SE reaction is the most favorable (based on their ΔG values), the energy profiles in Figure 3 are classified broadly as self-limiting or etching. The energy profile in Figure 3a is termed as “preferred self-limiting” since the SL reaction is more thermodynamically favored than the SE reaction, even though both SL and SE reactions are exergonic. Here, there is a possibility of etching if the collective barrier (at least $Y - X$) could be overcome under the reactor conditions. If the energy profile in Figure 3a is shifted along the vertical axis such that the SL reaction is exoergic and the SE reaction is endergonic, we obtain the energy profile in Figure 3b termed as “purely self-limiting”. This is the ideal energy profile for the surface modification pulse in an ALE process since unlimited etching is energetically unfavorable. The energy profile in Figure 3c is the reverse of that in Figure 3a since the SE reaction is energetically more favorable than the SL reaction ($Y - X < 0$). The collective barrier, if any, for etching would be comparatively lower than in the preferred self-limiting state, and it may be easily breached under the reactor conditions. Therefore, the energy profile in Figure 3c is termed as “preferred etching”. Figure 3d is obtained by shifting the energy profile in Figure 3c such that the SL reaction is endergonic and the SE reaction is exergonic. This profile is termed as “purely etching” since the precursor molecules should readily volatilize the surface atoms and proceed to the subsurface region to cause bulk etching without significant barriers. This is the ideal energy profile for a SE pulse. Thus, the shape of the energy profile at any given temperature and pressure will allow us to predict the net effect of the precursor–substrate interaction. We refer to this computational approach as the N–E analysis.

To summarize, by comparing the energetics and thermodynamics of the SE (bulk → gas) and SL (surf → surf) reactions, along with the

minimum energetic barrier separating them, we can predict whether the gas of a particular precursor pulse will spontaneously etch the substrate material at the temperatures and pressures of interest.

Bulk and Slab Models. We have optimized the bulk unit cell of monoclinic HfO_2 (space group: $P2_1/c$) and ZrO_2 (space group: $P2_1/c$) by simultaneously relaxing the ionic positions, cell shape, and cell volume with an energy cutoff of 550 eV and a Monkhorst–Pack k -point sampling mesh of $(6 \times 6 \times 6)$. The bulk monoclinic unit cells of HfO_2 and ZrO_2 have four metal atoms and eight O atoms. The optimized lattice constants of HfO_2 from this setup are $a = 5.142 \text{ \AA}$, $b = 5.195 \text{ \AA}$, and $c = 5.326 \text{ \AA}$, while the lattice constants of ZrO_2 are $a = 5.140 \text{ \AA}$, $b = 5.189 \text{ \AA}$, and $c = 5.239 \text{ \AA}$. Comparing our values to the experimental values for the baddeleyite phase,⁴³ the deviations for HfO_2 are $a = 0.43\%$, $b = 0.48\%$, and $c = 0.96\%$ and for ZrO_2 are $a = 0.58\%$, $b = 0.78\%$, and $c = 1.89\%$.

A surface slab of monoclinic HfO_2 and ZrO_2 with a (111) orientation is used for the surface calculations as this is the most stable facet at low temperatures and has the lowest surface energy.^{43,44} A surface supercell of HfO_2 and ZrO_2 with a (2×2) expansion of the hexagonal unit cell and 16 Å of vacuum separating the slabs is used for the surface models; this has a stoichiometry of $\text{Hf}_{80}/\text{Zr}_{80}\text{O}_{160}$ per supercell. It consists of five layers of 16 $\text{HfO}_2/\text{ZrO}_2$ units, and a k -point sampling mesh of $(2 \times 2 \times 1)$ is used for geometry optimization. The product states of the SL reactions needed for the N–E analysis are obtained by adding two F atoms per surface O removed (for brevity, we denote this ratio 1O/2F) from the top layer of the slab models. We consider three product states for our analysis: 8O/16F, 12O/24F, and 16O/32F. For the surface slabs, enthalpy H and entropy S are computed using the Phonopy code by considering only the first layer of atoms.⁴⁵ The calculations for the reactant molecules and gas-phase byproducts are performed in VASP with a large periodic box of dimensions $15.0 \text{ \AA} \times 16.0 \text{ \AA} \times 15.5 \text{ \AA}$ and 400 eV plane-wave energy cutoff. The enthalpy and entropy for the gas-phase molecules were calculated from the freeh program in the Turbomole suite⁴⁶ at 1 atm pressure. The above calculations are performed with the PBE exchange–correlation functional⁴¹ and a polarized triple ζ basis set (def-TZVPP)^{47,48} and default medium grid.

For the HF adsorption studies, the molecules are introduced at various surface sites and at different coverages on the (111) surface slabs of HfO_2 and ZrO_2 . The absorbate coverages and binding energies are computed, and a surface model with maximum coverage of metal–F is then used to derive the theoretical etch rate for the HF pulse on HfO_2 and ZrO_2 .

The VASP data can be found at the GitHub repository <https://github.com/RitaMull/Thermal-ALE-HfO2-and-ZrO2-with-HF>.

RESULTS

In the first part of this section, we will perform the N–E analysis and compare self-limiting with spontaneous etch

reaction models. In the next part, the adsorption mechanism of HF at a range of coverages on HfO_2 and ZrO_2 will be studied, together with analysis of H_2O formation. Finally, a theoretical etch rate is predicted based on the maximum possible coverage of dissociated HF on the material surfaces.

Self-Limiting vs Spontaneous Etch. Comparing the energetics and thermodynamics of the SL and SE model reactions for the fluorination of HfO_2 and ZrO_2 using HF, we can predict whether the HF pulse will spontaneously etch or result in a self-limiting reaction at the given conditions. Model reactions representing the HF pulse on HfO_2 and ZrO_2 are listed in Table 1 together with the corresponding reaction (free) energies at 0 and 500 K, with a reactant pressure of 0.2 Torr and a product pressure of 0.01 Torr, as computed from DFT calculations.

This table also includes the minimum barrier to cause spontaneous etch as already discussed. Negative minimum barriers indicate that spontaneous etch is thermodynamically favorable and is hindered only by kinetic barriers, if any. Two SE reactions and two SL reactions are postulated for HF exposure on both HfO_2 and ZrO_2 . The SE reactions involve the complete conversion of the bulk metal oxide into volatile metal fluoride (SE1) or metal oxyfluoride (SE2) and water, while the corresponding SL reactions involve conversion of the outermost surface layer of the metal oxide into the nonvolatile metal (oxy)fluoride (terminating the metal oxide), releasing water molecules. For the SE1 reaction of Hf/ZrO_2 , four HF molecules are needed to etch away one unit of bulk Hf/ZrO_2 to form Hf/ZrF_4 and H_2O . For the SE2 reaction for Hf/ZrO_2 , two HF molecules are required to etch a unit of Hf/ZrO_2 to form Hf/ZrOF_2 and H_2O . In the SE reactions, the surface of the material before and after each precursor pulse will be identical and therefore their contributions are ignored from the reaction model. For the SL reactions, the surfaces are not identical before and after the pulse and their contributions have to be included. In Table 1, the SL product state of the surfaces is 8O/16F (refer to Supporting Information (SI) for the geometry).

A negative reaction (free) energy (ΔG) means that the reaction is exergonic (favorable), and a positive ΔG means that the reaction is endergonic (unfavorable). The SE2 reactions forming volatile metal oxyfluorides are unfavorable at 0 and 500 K as the reaction (free) energy is positive (unfavorable), whereas the SE1 reactions forming volatile metal fluorides are favorable. For all of the SL–SE combinations at 0 K, for both materials, the minimum barrier to etch was positive, suggesting that self-limiting reaction is the most favorable energetically. At 500 K, the thermodynamic barrier is reduced considerably, which means high temperatures favor SE reactions. In any case, below 500 K, the minimum barrier is positive, suggesting that SL reactions are preferred for both metal oxides. Therefore, up to 500 K, the reactions are in preferred self-limiting state for both materials. Therefore, we can propose that the reaction of HF in the first step will self-limit on both metal oxides at least up to 500 K.

As the SE1 reactions forming the volatile metal fluoride are more favorable than the SE2 reactions that form the oxyfluoride, we will consider only the SE1 reactions for further analysis. Moreover, the barrier to etch was very high for the SL2–SE2 reactions as compared to the SL1–SE1, even at 500 K, suggesting that spontaneous formation of oxyfluoride is not probable at ALE-relevant temperatures.

Reaction Free Energy Profiles (FEPs). The free energy profiles (FEPs) of the reactions in Table 1 are discussed in this section. Comparing the reaction FEPs of the SE and SL reactions, we can determine at a given temperature and reactant pressure whether the HF pulse will favor spontaneous etching or self-limited conversion of HfO_2 and ZrO_2 into a nonvolatile metal fluoride layer. Here, we use a reactant pressure of 0.2 Torr and a product pressure of 0.01 Torr within a temperature range of 0–1000 K. The various contributions to the free energy for the example of the SE1 reaction for HfO_2 are plotted in Figure 4.

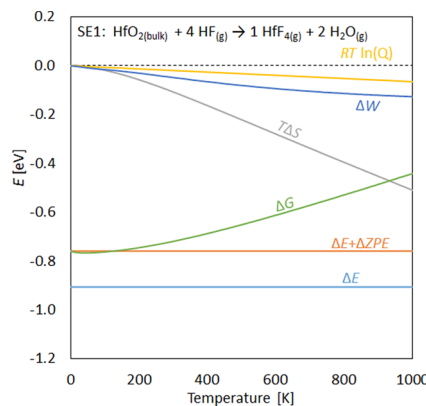


Figure 4. Contributions to the reaction FEP of the SE1 reaction of HfO_2 shown in Table 1. $RT \ln(Q)$ in gold accounts for the partial pressures of the reactants and products, enthalpic contribution (ΔW) is given in dark blue, entropy term ($T\Delta S$) in gray, reaction energy (ΔE) in light blue, the sum of reaction energy and zero-point energy change ($\Delta E + \Delta ZPE$) in brown, and reaction free energy (ΔG) in green.

In Figure 4, the ΔE and ΔZPE contributions are temperature independent. $T\Delta S$ is the entropy contribution and is 0 eV at 0 K and −0.5 eV at 1000 K. The entropy term decreases with increasing temperature because four gaseous reactant molecules result in the formation of three product molecules only. The $RT \ln(Q)$ and ΔW contributions are clearly smaller in comparison to the entropy term. They decrease the free energy at high temperatures and compete against the entropy term that increases the free energy with temperature. The FEP of this reaction at the reactant and product pressures stated above is exergonic up to 1000 K. The other reactions show similar contributions.

The FEPs of the SE1 and SL1 reactions of HfO_2 and ZrO_2 are compared in Figure 5. For HfO_2 , the self-limiting reaction is preferred up to 656 K. At 657 K, the SE1 and SL1 reactions are isoenergetic, with the minimum barrier becoming zero, and beyond this, the SE1 reaction is more favorable. Finally, at 813 K, the self-limiting reaction becomes endergonic and continuous etching dominates. We see similar trends for ZrO_2 , with self-limiting reactions preferred up to 533 K, while at 770 K, the self-limiting reaction becomes endergonic and continuous etching remains exergonic.

In Figure 5, the FEP is computed using the 8O/16F model as the SL product state. For completeness, we also determine the FEPs for two other SL product models, namely, 12O/24F and 16O/32F. Both surfaces of HfO_2 and ZrO_2 have 16 topmost O atoms (oxygen) in the supercell that could react with the HF molecules. For the 12O/24F product state, three-fourths of surface O are removed and 24 F (fluorine) are

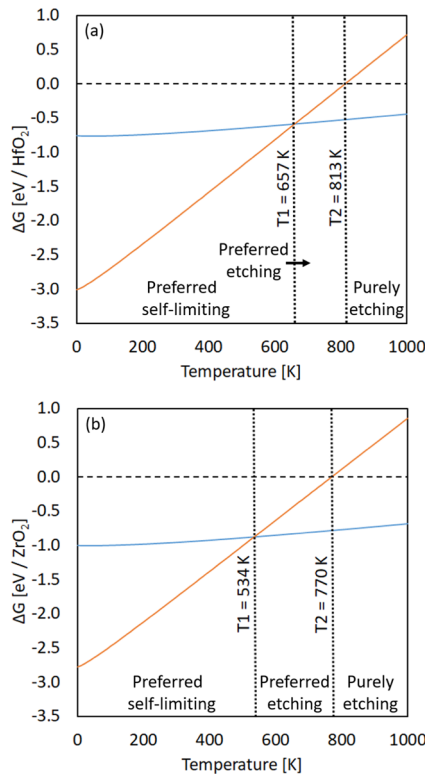


Figure 5. Free energy profiles for the SE1 (blue) and SL1 (orange) reactions of (a) HfO₂ and (b) ZrO₂ from 0 to 1000 K at the pressures given in the text. T_1 is where the self-limiting and spontaneous etch reactions cross over for the 8O/16F model, and T_2 is where spontaneous etching is preferred.

added to replace them. For the 16O/32F, all surface O are removed and 32 F are added to replace them. All oxygen atoms were removed as H₂O molecules. Basically, the M–O (M = Hf, Zr) coordination numbers of the surface metal atoms are decreasing from 8O/16F to 16O/32F. Note that the more O atoms are removed, the easier it would be to remove the surface metal atoms in the second pulse due to the reduced metal–O interaction. Therefore, we use the 12O/24F and 16O/32F product states merely as extreme test cases to compare their thermodynamic stability with the more reasonable 8O/16F model. The geometries used for the SL thermochemical calculations of both metal oxides are shown in Section S1 of the Supporting Information. Table 2 shows the energetics for the SL reactions including 12O/24F and 16O/32F models.

At 0 K, all SL reactions are more favorable than the SE reaction for both oxides and the minimum barriers are positive. For both oxides, we find the minimum barrier to decrease with the number of surface O atoms removed, with the lowest barriers for ZrO₂. At 500 K, the SL1 and SL2 reactions continue to be more favorable than the SE reaction, whereas the SL3 reaction is not. This means that an aggressive removal of surface O by HF during the first pulse would also enhance etching of the surface Hf/Zr atoms at ALE-relevant temperatures, say 500 K.

Experimental work showed that the HF reaction is self-limiting on HfO₂ at 200 °C (473 K),⁹ 250 °C (523 K),¹¹ and 300 °C (573 K).¹¹ Compared to Figure 6, this is true for partial surface O removal (8O/16F), where self-limiting is preferred up to 618 K for three-fourths of surface O removal

Table 2. Reaction (Free) Energies and Minimum Barriers within Parenthesis at 0 and 500 K for the Model SL Reactions Representing the HF Pulse on HfO₂ and ZrO₂ for 8O/16F, 12O/24F, and 16O/32F SL Product States (M = Hf, Zr)

SL product state	ΔE (0 K) (eV/M)	ΔG (500 K) (eV/M)
HfO₂		
SE1	HfF ₄	-0.91
SL1	8O/16F	-3.27 (2.36)
SL2	12O/24F	-3.05 (2.14)
SL3	16O/32F	-2.45 (1.54)
ZrO₂		
SE1	ZrF ₄	-1.14
SL1	8O/16F	-3.04 (1.90)
SL2	12O/24F	-2.91 (1.77)
SL3	16O/32F	-2.17 (1.03)

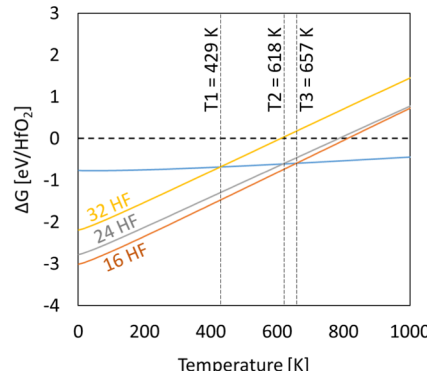


Figure 6. Free energy profiles of the continuous etching and self-limiting reactions for HfO₂. T_1 , T_2 , and T_3 are where the self-limiting and spontaneous etch reactions cross over for 16O/32F, 12O/24F, and 8O/16F models, respectively.

and up to 657 K for one half of surface O removal. The same analysis holds for ZrO₂ (Figure 7). Therefore, N–E analysis is

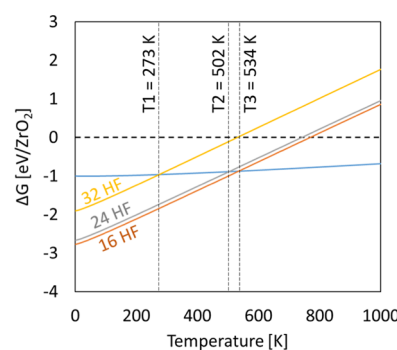


Figure 7. Free energy profiles of the continuous etching and self-limiting reactions for ZrO₂. T_1 , T_2 , and T_3 are where the self-limiting and spontaneous etch reactions cross over for 16O/32F, 12O/24F, and 8O/16F models, respectively.

a simple and relatively inexpensive method to predict the structure of the surface after the first ALE pulse. We will further validate this methodology on experimental results for different ALE processes in a future publication.

Adsorption of One HF Molecule at HfO₂ and ZrO₂. Kondati Natarajan and Elliott³⁹ studied the adsorption of HF on the bare surface of Al₂O₃ and found that Al–F bonding is

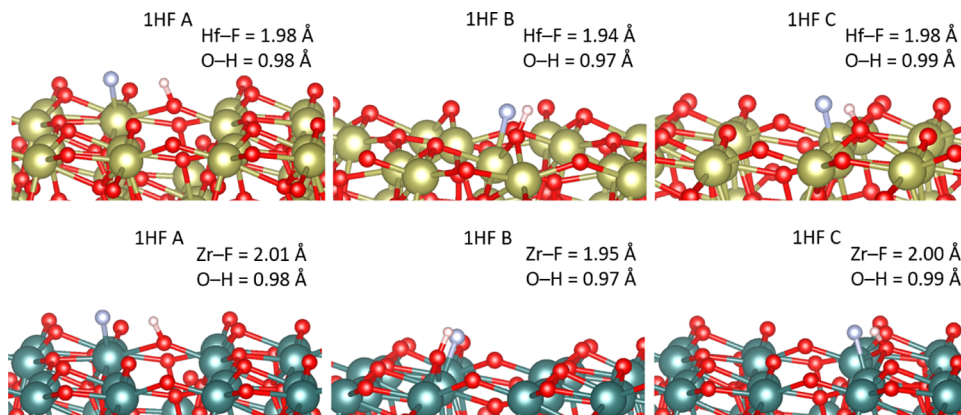


Figure 8. Relaxed adsorption structures for one HF molecule interacting with the bare surfaces of HfO_2 and ZrO_2 . The color coding is yellow = Hf, green = Zr, red = O, white = H, and blue = F.

crucial for HF dissociation. To find whether the same holds for HfO_2 and ZrO_2 , we adsorb one HF molecule to the optimized bare surfaces of both oxides at different binding sites (which we term A, B, and C). These sites were chosen to test whether molecular or dissociative adsorption of HF is sensitive to the adsorption site. The different binding sites for one HF are shown in Section S2 of the Supporting Information.

Figure 8 shows that the HF molecule is spontaneously dissociated at each binding site to form metal–F and O–H bonds on both oxides. No molecular HF adsorption was found. Similar to the Al_2O_3 case, we find that the HF dissociation proceeds after a stable M–F (M = Hf, Zr) bond is formed. The computed adsorption energies for the dissociative adsorption of one HF molecule on the bare surface of HfO_2 are -1.52 , -1.95 , and -1.63 eV at sites A, B, and C, respectively. The corresponding values for ZrO_2 are -1.25 , -1.74 , and -1.48 eV. The interaction between HfO_2 and HF is 0.15 – 0.21 eV stronger than between ZrO_2 and HF. The Hf–F, Zr–F, and O–H bond lengths are shown for each adsorption mode in Figure 8. The surface O atoms are either 2-fold or 3-fold coordinated by surface Hf/Zr atoms on both surfaces. All of the surface Hf/Zr atoms are 6-fold coordinated by O atoms. Since the structures of HfO_2 and ZrO_2 are similar, the strongest adsorption mode (one HF B for HfO_2 -1.95 eV and for ZrO_2 -1.74 eV) involves the same 6-fold coordinated metal lattice site and 2-fold coordinated surface oxygen site.

Stability of Different HF Coverages. The stability of different HF coverages was examined by introducing up to 34 randomly oriented HF molecules per supercell ca. 3 \AA from the bare monoclinic (111) surface of HfO_2 and ZrO_2 ; this results in coverages ranging from 1.0 ± 0.3 to 17.0 ± 0.3 HF/ nm^2 (2 HF to 34 HF molecules per supercell). There are 16 topmost metal atoms on the surface of the (2×2) supercell that may form metal–F bonds on both oxides. There are also 16 surface oxygen atoms on the bare surface of each metal oxide that can form O–H bonds or, as seen in some simulations, H_2O , which we discuss later. For each metal oxide, three different configurations (A, B, and C) were examined for the range of HF coverages using 2, 3, 4, 5, and 8 molecules per supercell and two configurations (A and B) using 12 and 16 molecules per supercell and one configuration for 30, 32, and 34 molecules per supercell. The computed energies of adsorption for the above-mentioned geometries are shown in Tables 3 and 4.

Table 3. Adsorbate Coverages and Binding Energies for the HF Coverages on the HfO_2 Surface Shown in Figure 9 and in Section S4 of the Supporting Information^a

HfO_2 geometry	coverage		E_{bind}	
	adsorbed HF (nm^{-2})	(Hf–F, dissociated F) (nm^{-2})	eV/HF	eV/ nm^2
2HF A (2, 2)	1.0	(1.0, 1.0)	-1.5	-1.5
2HF B (1, 1)	1.0	(0.5, 0.5)	-0.8	-0.8
2HF C (1, 1)	1.0	(0.5, 0.5)	-1.0	-1.0
3HF A (2, 2)	1.5	(1.0, 1.0)	-1.1	-1.7
3HF B (2, 2)	1.5	(1.0, 1.0)	-1.1	-1.6
3HF C (3, 3)	1.5	(1.5, 1.5)	-1.7	-2.6
4HF A (3, 3)	2.0	(1.5, 1.5)	-1.3	-2.6
4HF B (3, 3)	2.0	(1.5, 1.5)	-1.3	-2.7
4HF C (4, 4)	2.0	(2.0, 2.0)	-1.6	-3.2
5HF A (5, 5)	2.5	(2.5, 2.5)	-1.8	-4.6
5HF B (4, 4)	2.5	(2.0, 2.0)	-1.4	-3.4
5HF C (5, 5)	2.5	(2.5, 2.5)	-1.5	-3.7
8HF A (5, 4)	4.0	(2.5, 2.0)	-1.1	-4.6
8HF B (6, 6)	4.0	(3.0, 3.0)	-1.3	-5.2
8HF C (6, 5)	4.0	(3.0, 2.5)	-1.1	-4.4
12HF A (10, 7)	6.0	(5.0, 3.5)	-1.3	-7.7
12HF B (10, 7)	6.0	(5.0, 3.5)	-1.2	-7.3
16HF A (12, 8)	8.0	(6.0, 4.0)	-1.1	-9.0
16HF B (13, 9)	8.0	(6.5, 4.5)	-1.2	-9.6
30HF (12, 7)	15.0	(6.0, 3.5)	-0.8	-11.8
32HF (12, 6)	16.0	(6.0, 3.0)	-0.8	-12.1
34HF (14, 7)	17.0	(7.0, 3.5)	-0.9	-12.9

^aThe first number in parenthesis within the first column corresponds to the total number of Hf–F bonds, and the second number corresponds to the number of dissociated HF molecules. The most stable configurations, when more than one configuration is studied for a coverage, are highlighted in bold.

For HfO_2 , spontaneous complete dissociation of the adsorbed HF molecules was observed for some configurations with coverages of two, three, four, and five HF molecules, as shown in Figure 9. Similarly, for ZrO_2 , complete dissociation of adsorbed HF was seen for some configurations with coverages of two and four HF molecules only as shown in Figure 10. However, for the adsorption of three, five, and eight HF molecules on the ZrO_2 surface, upon relaxation, there were two, four, and seven dissociated HF molecules present for each configuration (A, B, or C); see Section S4 of the Supporting Information.

Table 4. Adsorbate Coverages and Binding Energies for the HF Coverages on the ZrO_2 Surface Shown in Figure 10 and in Section S4 of the Supporting Information^a

ZrO_2 geometry	coverage		E_{bind}	
	adsorbed HF (nm^{-2})	(Zr–F, dissociated F) (nm^{-2})	eV/HF	eV/ nm^2
2HF A (1, 1)	1.0	(0.5, 0.5)	-0.9	-0.9
2HF B (1, 1)	1.0	(0.5, 0.5)	-1.0	-1.0
2HF C (2, 2)	1.0	(1.0, 1.0)	-1.2	-1.2
3HF A (2, 2)	1.5	(1.0, 1.0)	-1.0	-1.6
3HF B (3, 2)	1.5	(1.5, 1.0)	-1.2	-1.9
3HF C (2, 2)	1.5	(1.0, 1.0)	-0.8	-1.2
4HF A (4, 4)	2.0	(2.0, 2.0)	-1.4	-2.6
4HF B (4, 4)	2.0	(2.0, 2.0)	-1.5	-3.1
4HF C (3, 3)	2.0	(1.5, 1.5)	-1.1	-2.2
SHF A (5, 4)	2.5	(2.5, 2.0)	-1.3	-3.2
SHF B (4, 4)	2.5	(2.0, 2.0)	-1.1	-2.8
SHF C (4, 4)	2.5	(2.0, 2.0)	-1.3	-3.3
8HF A (7, 7)	4.0	(3.5, 3.5)	-1.2	-5.0
8HF B (7, 7)	4.0	(3.5, 3.5)	-1.3	-5.1
8HF C (7, 7)	4.0	(3.5, 3.5)	-1.2	-4.9
12HF A (9, 6)	6.0	(4.5, 3.0)	-1.0	-6.0
12HF B (9, 7)	6.0	(4.5, 3.5)	-1.0	-6.3
16HF A (10, 8)	8.0	(5.0, 4.0)	-1.0	-7.9
16HF B (11, 7)	8.0	(5.5, 3.5)	-1.1	-8.6
30HF (13, 8)	15.0	(6.5, 4.0)	-0.8	-11.5
32HF (12, 6)	16.0	(6.0, 3.0)	-0.7	-11.5
34HF (13, 8)	17.0	(6.5, 4.0)	-0.7	-12.3

^aThe first number in parenthesis within the first column corresponds to the total number of Zr–F bonds, and the second number corresponds to the number of dissociated HF molecules. The most stable configurations, when more than one configuration is studied for a coverage, are highlighted in bold.

In all other HF adsorption configurations for HfO_2 and ZrO_2 , we find a mixture of molecular and dissociative adsorption of the HF molecules. We have computed binding energies per HF and per unit surface area of the material as listed in Tables 3 and 4.

For both metal oxides, the binding energy is more favorable as the extent of metal–F bonding increases on the bare surface. This can be seen for HfO_2 in Table 3 and Figure 11c with Hf–F coverage from 1.0 ± 0.3 to $7.0 \pm 0.3 \text{ nm}^{-2}$ with surface binding energies -1.5 to -12.9 eV/nm^2 . Similar trends are also

seen for ZrO_2 in Table 4 and Figure 12c with Zr–F coverage from 1.0 ± 0.3 to $6.5 \pm 0.3 \text{ nm}^{-2}$ with surface binding energies -0.9 to -12.3 eV/nm^2 . The HF molecules that did not dissociate in the relaxed geometries shown in Section S4 of the Supporting Information form hydrogen bonds with the remaining HF molecules and dissociated F atoms. For higher HF coverages, a more extensive hydrogen-bonded HF network is expected. There are intact HF molecules forming M–F bonds as well ($M = \text{Hf}, \text{Zr}$), whose coverage is found by subtracting the two numbers within parenthesis in Tables 3 and 4. These metal-bound HF molecules (M–FH) are not likely to be purged away in the next ALE step as they form strong bonds (Hf–F 6.7 eV and Zr–F 6.5 eV),⁴⁹ and these HF molecules should likely dissociate when the kinetic barriers are overcome inside the reactor. Therefore, we will use the total number of M–F bonds for the etch rate prediction in a later section.

Plot (a) in Figures 11 and 12 show scatter plots for metal–F coverage versus adsorbed HF coverage from the data in Tables 3 and 4 for HfO_2 and ZrO_2 , respectively. The dashed line shows a linear correlation between HF adsorption and metal–F coverage, which indicates the cases where all adsorbed HF molecules form metal–F bonds. The square data points along the dashed lines are those geometries where adsorbed HF coverage equals metal–F coverage. For HF adsorption at HfO_2 , this corresponds to the most stable configurations at coverages of $1.0, 1.5, 2.0$, and 2.5 HF/nm^2 . For ZrO_2 , this corresponds to the most stable configurations at coverages of 1.0 and 2.0 HF/nm^2 . Note that the data points of (2HF B and 2HF C), (3HF A and 3HF B), (4HF A and 4HF B), (5HF A and 5HF C), (8HF B and 8HF C), and (12HF A and 12HF B) overlap in Figure 11a as their adsorbed HF and Hf–F coverages are the same. Similarly, the data points of (2HF A and 2HF B), (3HF A and 3HF C), (4HF A and 4HF B), (5HF B and 5HF C), (8HF A and 8HF B and 8HF C), and (12HF A and 12HF B) overlap in Figure 12a. The points at higher HF coverages correspond to those geometries in which partially dissociated HF molecules are present, and hence, the points lie below the correlation line. As the HF coverage increases, the metal–F coverage starts to plateau, suggesting maximal coverages of $(6.0 \pm 0.3) - (7.0 \pm 0.3) \text{ metal–F/nm}^2$. Lee et al.⁹ found that for low HF coverages during etching of HfO_2 using HF and $\text{Sn}(\text{acac})_2$, there was a lack of self-limiting behavior as the HF reaction had not reached saturation. We

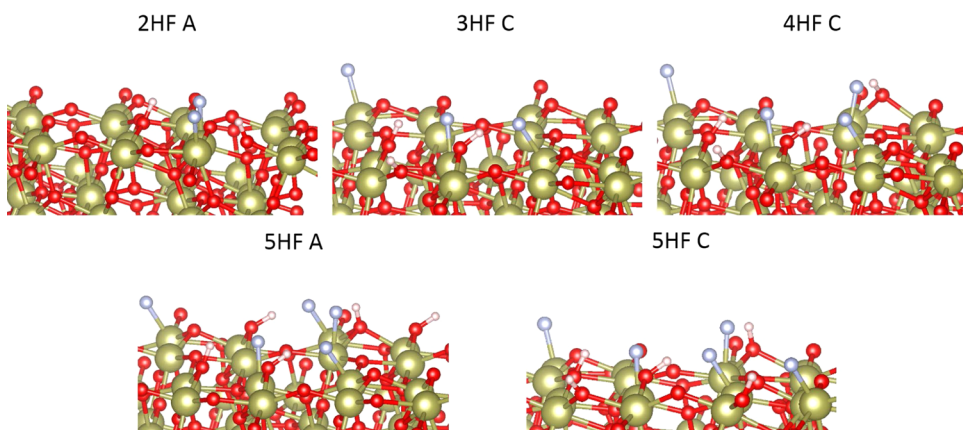


Figure 9. Relaxed geometries for HF coverages 2A, 3C, 4C, 5A, and 5C of HfO_2 where complete dissociation of HF occurred spontaneously. Color coding is the same as in Figure 8.

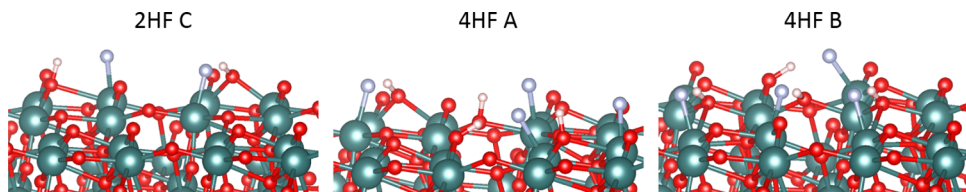


Figure 10. Relaxed geometries for HF coverages 2C, 4A, and 4B of ZrO_2 where complete dissociation of HF occurred spontaneously. Color coding is the same as in Figure 8.

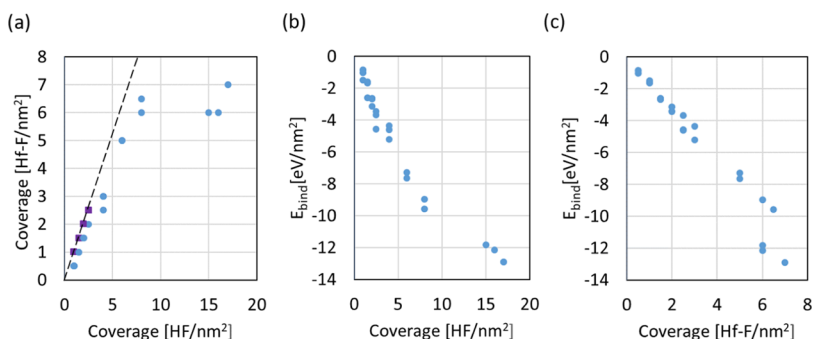


Figure 11. (a) Scatter plot for Hf–F coverage versus total HF coverage for the surface coverage values in Table 3. Note that some HF coverages resulted in partial or complete Hf–F coverage for different configurations, for example, the coverage of $1.0 \text{ HF}/\text{nm}^2$. The square data points are where the adsorbed HF coverage equals Hf–F coverage. The circular data points are where partially dissociated HF molecules are present. Plots (b) and (c) show the change in binding energy per square nanometer with an increase in HF and Hf–F coverage, respectively.

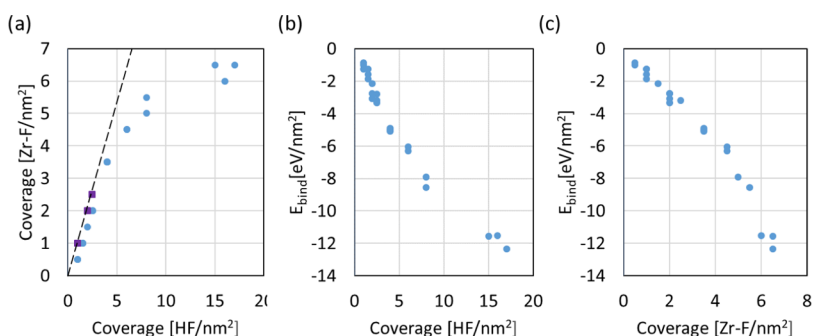


Figure 12. (a) Scatter plot for Zr–F coverage versus total HF coverage for the surface coverage values in Table 4. Note that some HF coverages resulted in partial or complete Zr–F coverage for different configurations, for example, the coverage of $1.0 \text{ HF}/\text{nm}^2$. The square data points are where the adsorbed HF coverage equals Zr–F coverage. The circular data points are where partially dissociated HF molecules are present. Plots (b) and (c) show the change in binding energy per square nanometer with an increase in HF and Zr–F coverage, respectively.

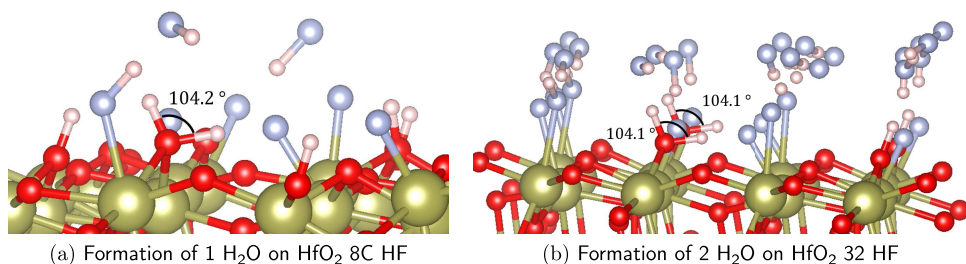


Figure 13. Relaxed fluorination geometries for HfO_2 that resulted in H_2O forming spontaneously. Color coding is the same as in Figure 8.

also find from plots (b) and (c) of Figures 11 and 12 that a saturation in the binding energy is not reached even at high HF coverages. Therefore, the highest adsorbed HF coverage of 34 HF with M–F coverages ($M = \text{Hf}, \text{Zr}$) of 7.0 ± 0.3 and $6.5 \pm 0.3 \text{ metal-F}/\text{nm}^2$ will be used as the maximum coverage for the HfO_2 and ZrO_2 etch rate prediction, respectively. We added an exponential fit to the data in plot (b) of Figures 11

and 12 in Section S6 of SI along with its derivative, which provides HF addition energy indirectly.

Water Formation. The spontaneous formation of H_2O was observed in some of our relaxed geometries for the examples of 8C ($3.0 \pm 0.3 \text{ Hf-F}/\text{nm}^2$) on HfO_2 and 16A ($5.0 \pm 0.3 \text{ Zr-F}/\text{nm}^2$) on ZrO_2 . The atomic structures are shown in Figure 13, where dissociation of at least two HF molecules provides the hydrogen atoms required to form H_2O as a

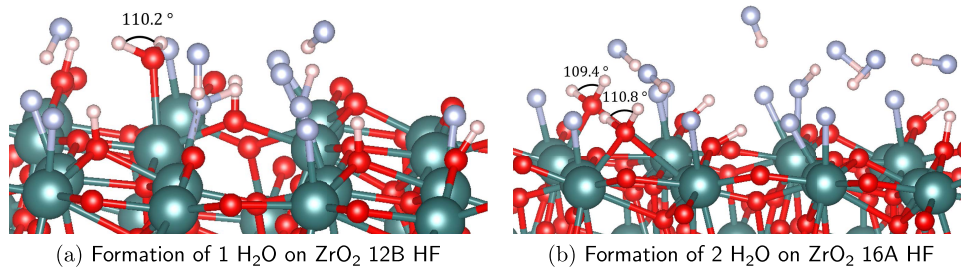


Figure 14. Relaxed fluorination geometries for ZrO_2 that resulted in H_2O forming spontaneously. Color coding is the same as in Figure 8.

reaction product, which removes oxygen from HfO_2 , as discussed in ref 9, but not discussed to date for ZrO_2 . H_2O formation on the HfO_2 surface was observed on geometries 8HF C and 32HF, in which the $\text{H}-\text{O}-\text{H}$ bond angle is 104.2° . Similarly, H_2O formation on the ZrO_2 surface was observed on geometries 12HF B and 16HF A HF as shown in Figure 14. The $\text{H}-\text{O}-\text{H}$ bond angle is 110.2° for 12HF B, and for 16HF A, it is 109.4 and 110.8° .

The energy to remove H_2O (energy of desorption) from the fluorinated surfaces of 8HF C and 32HF for HfO_2 and 12HF B and 16HF A for ZrO_2 was calculated using eq 9

$$E_{\text{des}} = (E_{\text{HfO}_2(\text{surf})/\text{HF}(\text{ads})} + E_{\text{H}_2\text{O}_{(\text{g})}}) - (E_{\text{HfO}_2(\text{surf})/\text{HF}(\text{ads})/\text{H}_2\text{O}_{(\text{ads})}}) \quad (9)$$

The term “ $E_{\text{HfO}_2(\text{surf})/\text{HF}(\text{ads})/\text{H}_2\text{O}_{(\text{ads})}}$ ” is the total energy of HF adsorbed on HfO_2 with spontaneous H_2O formation. H_2O was removed from the fluorinated metal oxide surface with unbound HF molecules, and the resulting geometry was relaxed. The term “ $E_{\text{HfO}_2(\text{surf})/\text{HF}(\text{ads})}$ ” is the total energy of HF adsorbed on HfO_2 after removing H_2O from the surface, and “ $E_{\text{H}_2\text{O}_{(\text{g})}}$ ” is the energy of a gas-phase H_2O molecule. The desorption energies of H_2O are presented in Table 5. These energies are relatively low and can be achievable at process conditions to remove surface-bound H_2O .

Table 5. List of Configurations That Resulted in Barrierless H_2O Formation and the Energy Required to Remove H_2O from Their Surface

configuration	no. H_2O formed	$E_{(\text{des})}$ (eV/ H_2O)
		HfO ₂
8C HF	1	0.70
32 HF	2	1.32
		ZrO ₂
12 HF	1	1.30
16A HF	2	0.50

■ DISCUSSION

From the N–E analysis, at all $T < 500$ K using reactant and product pressures of 0.2 and 0.01 Torr, respectively, and an 8O/16F surface model as the SL product state, the HF pulse on HfO_2 and ZrO_2 is self-limiting in nature, as the reaction energies for the self-limiting reactions were more favorable than the spontaneous etching reactions. Therefore, we suggest that the first precursor pulse using HF, at these conditions, will produce a stable and nonvolatile layer of metal fluorides and H_2O as byproducts. We also found that at elevated temperatures, the formation of the volatile metal fluoride is more favorable than the formation of the volatile metal

oxyfluoride. The self-limiting nature of the fluorination reaction is due to the formation of a passivated layer during HF exposure.²⁶ The HfF_x layer formed on HfO_2 after fluorination is self-limiting because this surface layer forms a diffusion barrier to subsequent fluorination by HF.¹¹ Multiple coverages of HF molecules starting from 1.0 ± 0.3 to 17.0 ± 0.3 HF/nm² resulted in mixed dissociated and molecular adsorption of HF to the surfaces of HfO_2 and ZrO_2 . We found maximal coverages of $(6.0 \pm 0.3)-(7.0 \pm 0.3)$ metal–F/nm² at higher HF coverages. Water forms spontaneously on relaxation from some of the geometries for multiple HF adsorption for both HfO_2 and ZrO_2 . The computed desorption energies to remove H_2O from our fluorinated surfaces of HfO_2 and ZrO_2 are low enough to be overcome at process conditions.

For both HfO_2 and ZrO_2 , the surfaces with an initial coverage of 17.0 ± 0.3 HF/nm² that resulted in 7.0 ± 0.3 Hf–F/nm² and 6.5 ± 0.3 Zr–F/nm², respectively, are used to calculate a theoretical etch rate. Both (2×2) supercells of monoclinic (111) HfO_2 and ZrO_2 have surface areas of 1.98 nm² with 16 metal atoms on the surface that can form metal–F bonds that correspond to coverages of 8.0 ± 0.3 Hf/nm² and 8.0 ± 0.3 Zr/nm², respectively. As the maximum coverage of Hf–F is 7.0 ± 0.3 F/nm², there will be approximately 0.88 F atoms per surface Hf. The maximum coverage of Zr–F is 6.5 ± 0.3 F/nm², so there will be approximately 0.81 F atoms per surface Zr. The SE1 reactions showed that four F atoms lead to the etching of one Hf/Zr atom as volatile metal tetrafluoride. Similar to the analysis done by Kondati Natarajan et al.,³⁹ the coverage of Hf/Zr that can be etched is one-quarter of the M–F coverage ($M = \text{Hf}, \text{Zr}$), 1.8 ± 0.1 Hf/(nm² cycle) for HfO_2 and 1.6 ± 0.1 Zr/(nm² cycle) for ZrO_2 . As the surface concentration of metal atoms is 8.0 ± 0.3 Hf or Zr/nm², this etch rate corresponds to 0.2 monolayer/cycle. For HfO_2 , this corresponds to -61.2 ± 0.8 ng/(cm² cycle) and using the mass density of bulk HfO_2 (10.0 g/cm³), -0.61 ± 0.02 Å/cycle. For ZrO_2 , this corresponds to -33.3 ± 0.8 ng/(cm² cycle) and using the mass density of bulk ZrO_2 (5.9 g/cm³), -0.57 ± 0.02 Å/cycle. It is important to note that these computed etch rates do not take into account kinetic effects that would be included in experimental etch rates. Therefore, we also compute the maximum etch rate for the removal of a complete monolayer of material from HfO_2 and ZrO_2 . We used 16 metal atoms for one ML removal, which requires a Hf–F/Zr–F coverage of 32.32 ± 0.3 F/nm². An etch rate of -2.82 ± 0.02 Å/cycle was computed for one ML removal using the same method for calculating the theoretical etch rate. Therefore, if the etch rate is greater than -2.82 ± 0.02 Å/cycle, then it suggests that subsurface metal atoms are being etched.

A summary of experimental etch rates for HfO_2 and ZrO_2 using HF and a metal precursor is shown in Section S5 of the

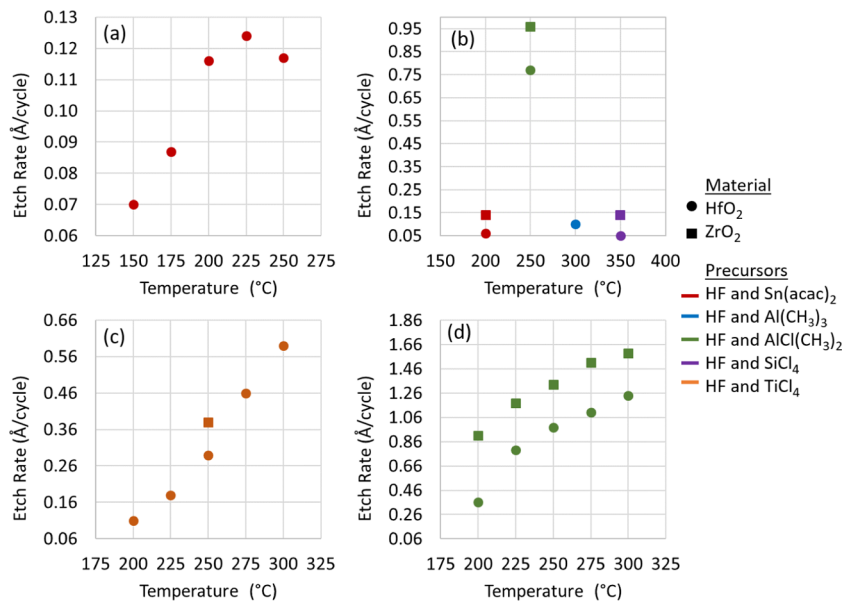


Figure 15. Experimental etch rates for the thermal ALE of HfO₂ and ZrO₂ using precursors HF and Sn(acac)₂,^{4,9} Al(CH₃)₃,⁴ AlCl(CH₃)₂,^{4,12} SiCl₄,⁴ and TiCl₄.¹¹¹¹ (a) Etch rates for the thermal ALE of HfO₂ using HF and Sn(acac)₂ for the temperature range of 150–250 °C. (b) Etch rates for the thermal ALE of HfO₂ and ZrO₂ using HF and Sn(acac)₂/AlCl(CH₃)₂/Al(CH₃)₃/SiCl₄ at the temperatures shown. (c) Etch rates for the thermal ALE using HF and TiCl₄ of HfO₂ for the temperature range 200–300 °C and ZrO₂ at 250 °C. (d) Etch rates for the thermal ALE of HfO₂ and ZrO₂ using HF and AlCl(CH₃)₂ for the temperature range 200–300 °C.

Supporting Information and also in Figure 15. The first thing we observe is that for a specific reactant combination, the etch rate increases with temperature for both materials and the etch rate for ZrO₂ is larger than that of HfO₂. We have predicted this from N–E analysis that the minimum barrier to continuous etching decreases considerably with an increase in temperature, more so in the case of ZrO₂ when compared to HfO₂. Between 150 and 350 °C, for different reactant combinations, the etch rates can be anywhere between 0.05 and 1.24 Å/cycle for HfO₂ and between 0.01 and 1.59 Å/cycle for ZrO₂. The computed etch rate prediction given earlier based on the maximal M–F coverage (M = Hf, Zr) should be taken carefully as the experimental etch rate varies greatly with temperature and the reactant, in the second pulse. Moreover, the maximal experimental etch rate reported is much larger than the predicted etch rate, suggesting that further reaction of adsorbed HF with the substrate is possible and this reaction surmounts the kinetic barriers, which we have not included in this simple adsorption study. However, comparing the maximal etch rate of -2.82 ± 0.02 Å/cycle for one ML removal of Hf/ZrO₂ along with experimental etch rates, we can calculate the number of Hf/Zr removed/nm² in those experiments. Our surface model contains 8.0 ± 0.3 M/nm² (M = Hf, Zr) as mentioned earlier. Therefore, an etch rate of -2.82 ± 0.02 Å/cycle corresponds to a removal of 8.0 ± 0.3 M/nm² of the surface. Thus

$$\text{no. of metal atoms removed/nm}^2 = \text{expt. etch rate} \times \left(-\frac{8.0}{2.8} \pm 0.1 \right) \quad (10)$$

For example, 4.5 ± 0.1 Zr atoms/nm² are removed as volatile ZrF₄ per cycle for an experimental etch rate of 1.59 Å/cycle using HF and DMAc at 300 °C. These results are also listed in Section S5 of the Supporting Information. It is clear that in all of these experiments, less than a monolayer of material is removed per ALE cycle. This computational approach detailed

in this paper provides a general guideline to safely examine the influence of any reactant species on the substrate materials of interest.

CONCLUSIONS

We present DFT calculations to understand the nature of the HF pulse on the bare surfaces of monoclinic HfO₂ and ZrO₂ for thermal ALE. N–E analysis of the self-limiting and spontaneous (continuous) etching using simple reaction models representing the HF exposure on HfO₂ and ZrO₂ allowed us to predict whether SL or SE reaction is favorable at a given temperature and at a given pressure. At $T < 500$ K, the HF reaction with both oxides is found to be in the preferred self-limiting state. This is a relatively inexpensive way to screen the reactant molecules for ALE, also equally applicable to ALD, of any given substrate. We studied the adsorption of HF molecules on HfO₂ and ZrO₂ for HF coverages ranging from 1.0 ± 0.3 to 17.0 ± 0.3 HF/nm² along with analysis of H₂O formation. From this analysis, we predict a theoretical etch rate based on the maximum possible coverage of surface-bound HF for HfO₂ and ZrO₂. The maximal computed metal–F coverage on both surfaces is from 6.0 ± 0.3 to 7.0 ± 0.3 metal–F/nm². The spontaneous formation of water was also seen at some HF coverages on both oxides. We calculated theoretical etch rates of -0.61 ± 0.02 Å/cycle for HfO₂ and -0.57 ± 0.02 Å/cycle for ZrO₂, which are lower than the maximal etch rates reported from experiments. The etch rate for a complete ML removal, -2.82 ± 0.02 Å/cycle, was used with experimental etch rates to compute the number of metal atoms removed from the surface per square nanometer per cycle. We can use the presented methodology for the first pulse on HfO₂ and ZrO₂ to examine other reagents such as HCl and HBr with a similar analysis as well as examine the interaction of HF on hydroxyl-terminated surfaces of HfO₂ and ZrO₂.

■ ASSOCIATED CONTENT

SI Supporting Information

The Supporting Information is available free of charge at <https://pubs.acs.org/doi/10.1021/acs.chemmater.9b05021>.

Self-limiting surface models used for thermochemical analysis, binding sites of one HF molecule at HfO_2 and ZrO_2 in HF adsorption studies, summary of bond dissociation energies, mixed molecular and dissociative adsorption of HF molecules from HF adsorption studies, experimental etch rates of HfO_2 and ZrO_2 with the corresponding number of metal atoms removed per square nanometer, and addition energy from increasing HF coverages ([PDF](#))

■ AUTHOR INFORMATION

Corresponding Author

Michael Nolan — Tyndall National Institute, University College Cork, Cork T12 RSCP, Ireland;  [orcid.org/0000-0002-5224-8580](#); Email: michael.nolan@tyndall.ie

Authors

Rita Mullins — Tyndall National Institute, University College Cork, Cork T12 RSCP, Ireland;  [orcid.org/0000-0002-3898-7328](#)

Suresh Kondati Natarajan — Tyndall National Institute, University College Cork, Cork T12 RSCP, Ireland; Department of Electrical Engineering and Automation, Aalto University, Espoo 02150, Finland;  [orcid.org/0000-0002-7018-5253](#)

Simon D. Elliott — Schrödinger Inc., New York, New York 10036-4041, United States;  [orcid.org/0000-0001-5573-5694](#)

Complete contact information is available at: <https://pubs.acs.org/10.1021/acs.chemmater.9b05021>

Author Contributions

[†]R.M. and S.K.N. contributed equally to this manuscript.

Notes

The authors declare no competing financial interest.

■ ACKNOWLEDGMENTS

We acknowledge support for this work from LAM Research and the Science Foundation Ireland—NSF China Partnership Program, NITRALD Grant number: 17/NSFC/5279. We are grateful for access to Tyndall computing facilities supported by SFI and the Irish Centre for High-End Computing, www.ichec.ie.

■ REFERENCES

- (1) Raghu, P.; Yim, C.; Shadman, F.; Sher, E. Susceptibility of SiO_2 , ZrO_2 , and HfO_2 dielectrics to moisture contamination. *AIChE J.* **2004**, *50*, 1881–1888.
- (2) Raghu, P.; Rana, N.; Yim, C.; Sher, E.; Shadman, F. Adsorption of Moisture and Organic Contaminants on Hafnium Oxide, Zirconium Oxide, and Silicon Oxide Gate Dielectrics. *J. Electrochem. Soc.* **2003**, *150*, No. F186.
- (3) Hausmann, D. M.; Kim, E.; Becker, J.; Gordon, R. G. Atomic Layer Deposition of Hafnium and Zirconium Oxides Using Metal Amide Precursors. *Chem. Mater.* **2002**, *14*, 4350–4358.
- (4) Lee, Y.; Huffman, C.; George, S. M. Selectivity in Thermal Atomic Layer Etching Using Sequential, Self Limiting Fluorination and Ligand-Exchange Reactions. *Chem. Mater.* **2016**, *28*, 7657–7665.
- (5) Oehrlein, G. S.; Metzler, D.; Li, C. Atomic Layer Etching at the Tipping Point: An Overview. *ECS J. Solid State Sci. Technol.* **2015**, *4*, N5041.
- (6) Kanarik, K. J.; Lill, T.; Hudson, E. A.; Sriraman, S.; Tan, S.; Marks, J.; Vahedi, V.; Gottsch, R. A. Overview of atomic layer etching in the semiconductor industry. *J. Vac. Sci. Technol., A* **2015**, *33*, No. 020802.
- (7) George, S. M.; Lee, Y. Prospects for Thermal Atomic Layer Etching Using Sequential, Self-Limiting Fluorination and Ligand-Exchange Reactions. *ACS Nano* **2016**, *10*, 4889–4894.
- (8) Yuan, G.; Wang, N.; Huang, S.; Liu, J. In *A Brief Overview of Atomic Layer Deposition and Etching in the Semiconductor Processing*, 2016 17th International Conference on Electronic Packaging Technology (ICEPT), 2016; pp 1365–1368.
- (9) Lee, Y.; DuMont, J. W.; George, S. M. Atomic Layer Etching of HfO_2 Using Sequential, Self-Limiting Thermal Reactions with $\text{Sn}(\text{acac})_2$ and HF. *ECS J. Solid State Sci. Technol.* **2015**, *4*, N5013.
- (10) Lee, Y.; George, S. M. Atomic Layer Etching of Al_2O_3 Using Sequential, Self-Limiting Thermal Reactions with $\text{Sn}(\text{acac})_2$ and Hydrogen Fluoride. *ACS Nano* **2015**, *9*, 2061–2070.
- (11) Lee, Y.; George, S. M. Thermal atomic layer etching of HfO_2 using HF for fluorination and TiCl_4 for ligand-exchange. *J. Vac. Sci. Technol., A* **2018**, *36*, No. 061504.
- (12) Lee, Y.; George, S. M. Thermal Atomic Layer Etching of Al_2O_3 , HfO_2 , and ZrO_2 Using Sequential Hydrogen Fluoride and Dimethylaluminum Chloride Exposures. *J. Phys. Chem. C* **2019**, *123*, 18455–18466.
- (13) DuMont, J. W.; Marquardt, A. E.; Cano, A. M.; George, S. M. Thermal Atomic Layer Etching of SiO_2 by a Conversion-etch Mechanism Using Sequential Reactions of Trimethylaluminum and Hydrogen Fluoride. *ACS Appl. Mater. Interfaces* **2017**, *9*, 10296–10307.
- (14) Lee, Y.; DuMont, J. W.; George, S. M. Mechanism of Thermal Al_2O_3 Atomic Layer Etching Using Sequential Reactions with $\text{Sn}(\text{acac})_2$ and HF. *Chem. Mater.* **2015**, *27*, 3648.
- (15) Lee, Y.; George, S. M. Atomic Layer Etching of Al_2O_3 Using Sequential, Self-Limiting Thermal Reactions with $\text{Sn}(\text{acac})_2$ and Hydrogen Fluoride. *ACS Nano* **2015**, *9*, 2061–2070.
- (16) Lee, Y.; DuMont, J. W.; George, S. M. Trimethylaluminum as the Metal Precursor for the Atomic Layer Etching of Al_2O_3 Using Sequential, Self-Limiting Thermal Reactions. *Chem. Mater.* **2016**, *28*, 2994.
- (17) Hennessy, J.; Moore, C. S.; Balasubramanian, K.; Jewell, A. D.; France, K.; Nikzad, S. Enhanced atomic layer etching of native aluminum oxide for ultraviolet optical applications. *J. Vac. Sci. Technol., A* **2017**, *35*, No. 041512.
- (18) DuMont, J. W.; George, S. M. Competition between Al_2O_3 atomic layer etching and AlF_3 atomic layer deposition using sequential exposures of trimethylaluminum and hydrogen fluoride. *J. Chem. Phys.* **2017**, *146*, No. 052819.
- (19) Johnson, N. R.; Sun, H.; Sharma, K.; George, S. M. Thermal atomic layer etching of crystalline aluminum nitride using sequential, self-limiting hydrogen fluoride and $\text{Sn}(\text{acac})_2$ reactions and enhancement by H_2 and Ar plasmas. *J. Vac. Sci. Technol., A* **2016**, *34*, No. 050603.
- (20) Lee, Y.; DuMont, J. W.; George, S. M. Atomic Layer Etching of AlF_3 Using Sequential, Self-Limiting Thermal Reactions with $\text{Sn}(\text{acac})_2$ and Hydrogen Fluoride. *J. Phys. Chem. C* **2015**, *119*, 25385–25393.
- (21) Lemaire, P. C.; Parsons, G. N. Thermal Selective Vapor Etching of TiO_2 : Chemical Vapor Etching via WF_6 and Self-Limiting Atomic Layer Etching Using WF_6 and BCl_3 . *Chem. Mater.* **2017**, *29*, 6653–6665.
- (22) Lee, Y.; George, S. M. Thermal Atomic Layer Etching of Titanium Nitride Using Sequential, Self-Limiting Reactions: Oxidation to TiO_2 and Fluorination to Volatile TiF_4 . *Chem. Mater.* **2017**, *29*, 8202–8210.
- (23) Shinoda, K.; Miyoshi, N.; Kobayashi, H.; Izawa, M.; Ishikawa, K.; Hori, M. Rapid thermal-cyclic atomic-layer etching of titanium

- nitride in CHF_3/O_2 downstream plasma. *J. Phys. D: Appl. Phys.* **2019**, *52*, No. 475106.
- (24) Xie, W.; Lemaire, P. C.; Parsons, G. N. Thermally Driven Self-Limiting Atomic Layer Etching of Metallic Tungsten Using WF_6 and O_2 . *ACS Appl. Mater. Interfaces* **2018**, *10*, 9147–9154.
- (25) Johnson, N. R.; George, S. M. WO_3 and W Thermal Atomic Layer Etching Using Conversion-Fluorination and Oxidation-Conversion-Fluorination Mechanisms. *ACS Appl. Mater. Interfaces* **2017**, *9*, 34435–34447.
- (26) Zytwotko, D. R.; George, S. M. Thermal Atomic Layer Etching of ZnO by a Conversion-Etch Mechanism Using Sequential Exposures of Hydrogen Fluoride and Trimethylaluminum. *Chem. Mater.* **2017**, *29*, 1183–1191.
- (27) Johnson, N. R.; Hite, J. K.; Mastro, M. A.; Eddy, C. R.; George, S. M. Thermal atomic layer etching of crystalline GaN using sequential exposures of XeF_2 and BCl_3 . *Appl. Phys. Lett.* **2019**, *114*, No. 243103.
- (28) Lim, W. S.; Park, J. B.; Park, J. Y.; Park, B. J.; Yeom, G. Y. Low damage atomic layer etching of ZrO_2 by using BCl_3 gas and ar neutral beam. *J. Nanosci.* **2009**, *9*, 7379–7382.
- (29) Dallorto, S.; Goodyear, A.; Cooke, M.; Szornel, J. E.; Ward, C.; Kastl, C.; Schwartzberg, A.; Rangelow, I. W.; Cabrini, S. Atomic layer etching of SiO_2 with Ar and CHF_3 plasmas: A self-limiting process for aspect ratio independent etching. *Plasma Process Polym.* **2019**, *16*, No. 1900051.
- (30) Koh, K.; Kim, Y.; Kim, C.-K.; Chae, H. Quasi atomic layer etching of SiO_2 using plasma fluorination for surface cleaning. *J. Vac. Sci. Technol., A* **2018**, *36*, No. 01B106.
- (31) Mameli, A.; Verheijen, M. A.; Mackus, A. J. M.; Kessels, W. M. M.; Roozeboom, F. Isotropic Atomic Layer Etching of ZnO Using Acetylacetone and O_2 Plasma. *ACS Appl. Mater. Interfaces* **2018**, *10*, 38588–38595.
- (32) Ohba, T.; Yang, W.; Tan, S.; Kanarik, K.; Nojiri, K. Atomic layer etching of GaN and AlGaN using directional plasma-enhanced approach. *Jpn. J. Appl. Phys.* **2017**, *56*, No. 06HB06.
- (33) Kauppinen, C.; Khan, S. A.; Sundqvist, J.; Suyatin, D. B.; Suihkonen, S.; Kauppinen, E. I.; Sopanen, M. Atomic layer etching of gallium nitride (0001). *J. Vac. Sci. Technol., A* **2017**, *35*, No. 060603.
- (34) Miyoshi, N.; Kobayashi, H.; Shinoda, K.; Kurihara, M.; Watanabe, T.; Kouzuma, Y.; Yokogawa, K.; Sakai, S.; Izawa, M. Atomic layer etching of silicon nitride using infrared annealing for short desorption time of ammonium fluorosilicate. *Jpn. J. Appl. Phys.* **2017**, *56*, No. 06HB01.
- (35) Lu, W.; Lee, Y.; Gertsch, J. C.; Murdzek, J. A.; Cavanagh, A. S.; Kong, L.; del Alamo, J. A.; George, S. M. In Situ Thermal Atomic Layer Etching for Sub-5 nm InGaAs Multigate MOSFETs. *Nano Lett.* **2019**, *19*, 5159–5166.
- (36) Gertsch, J. C.; Cano, A. M.; Bright, V. M.; George, S. M. SF_4 as the Fluorination Reactant for Al_2O_3 and VO_2 Thermal Atomic Layer Etching. *Chem. Mater.* **2019**, *31*, 3624–3635.
- (37) Rahman, R.; Mattson, E. C.; Klesko, J. P.; Dangerfield, A.; Rivillon-Amy, S.; Smith, D. C.; Hausmann, D.; Chabal, Y. J. Thermal Atomic Layer Etching of Silica and Alumina Thin Films Using Trimethylaluminum with Hydrogen Fluoride or Fluoroform. *ACS Appl. Mater. Interfaces* **2018**, *10*, 31784–31794.
- (38) Fang, C.; Cao, Y.; Wu, D.; Li, A. Thermal atomic layer etching: Mechanism, materials and prospects. *Prog. Nat. Sci.: Mater. Int.* **2018**, *28*, 667–675.
- (39) Kondati Natarajan, S.; Elliott, S. D. Modeling the Chemical Mechanism of the Thermal Atomic Layer Etch of Aluminum Oxide: A Density Functional Theory Study of Reactions during HF Exposure. *Chem. Mater.* **2018**, *30*, 5912–5922.
- (40) Kresse, G.; Furthmuller, J. Efficient iterative schemes for ab initio total-energy calculations using a plane-wave basis set. *Phys. Rev. B* **1996**, *54*, 11169.
- (41) Perdew, J. P.; Burke, K.; Ernzerhof, M. Generalized gradient approximation made simple. *Phys. Rev. Lett.* **1996**, *77*, 3865.
- (42) Kresse, G.; Joubert, D. From ultrasoft pseudopotentials to the projector augmented-wave method. *Phys. Rev. B* **1999**, *59*, 1758.
- (43) Lowther, J. E.; Dewhurst, J. K.; Leger, J. M.; Haines, J. Relative stability of ZrO_2 and HfO_2 structural phases. *Phys. Rev. B* **1999**, *60*, 14485–14488.
- (44) Zhao, X.; Vanderbilt, D. First-principles study of structural, vibrational, and lattice dielectric properties of hafnium oxide. *Phys. Rev. B* **2002**, *65*, No. 233106.
- (45) Togo, A.; Tanaka, I. First principles phonon calculations in materials science. *Scr. Mater.* **2015**, *108*, 1–5.
- (46) TURBOMOLE v6.2 2010, A Development of University of Karlsruhe and Forschungszentrum Karlsruhe GmbH, 1989–2007, TURBOMOLE GmbH, since 2007. Available from <http://www.turbomole.com> (last accessed 27 Nov, 2019).
- (47) Schäfer, A.; Huber, C.; Ahlrichs, R. Fully optimized contracted Gaussian basis sets of triple zeta valence quality for atoms Li to Kr. *J. Chem. Phys.* **1994**, *100*, 5829–5835.
- (48) Schäfer, A.; Horn, H.; Ahlrichs, R. Fully optimized contracted Gaussian basis sets for atoms Li to Kr. *J. Chem. Phys.* **1992**, *97*, 2571–2577.
- (49) Luo, Y. R. *Comprehensive Handbook of Chemical Bond Energies*; CRC Press: Boca Raton, FL, 2007.